Journal of The
Electrochemical Society

Design and Performance of the BYD LFP/Graphite 4680 Cylindrical Cell

To cite this article: Alex Liu *et al* 2025 *J. Electrochem. Soc.* **172** 110536

Journal of The Electrochemical Society, 2025 **172** 110536

Design and Performance of the BYD LFP/Graphite 4680 Cylindrical Cell

Alex Liu,[1] Weiliang Yao,[2] Shaojie Yang,[3] David Gonsoulin,[4] Aiden Larson,[1] Amariah Condon,[5] Peter M. Attia,[5,*,z] and Ying Shirley-Meng[1,6,,z]**

[1]*Aiiso Yufeng Li Family Department of Chemical and Nano Engineering, University of California, San Diego, La Jolla, California 92093, United States of America*
[2]*Department of Materials Science and Engineering, University of California, San Diego, La Jolla, California 92093, United States of America*
[3]*Department of Mechanical and Aerospace Engineering, University of California, San Diego, La Jolla, California 92093, United States of America*
[4]*Center for Energy Research, University of California, San Diego, La Jolla, CA 92093, United States of America*
[5]*Glimpse, Somerville, Massachusetts 02143, United States of America*
[6]*Pritzker School of Molecular Engineering, University of Chicago, Chicago, Illinois 60637, United States of America*

The increasing demand for large-format lithium-ion batteries in electric vehicles has accelerated the development of cell formats that offer higher energy density and improved pack-level efficiency. Among these, the 4680 cylindrical cell format, pioneered by Tesla, has gained widespread adoption due to its potential to simplify battery pack architecture while enhancing gravimetric energy density. Other cell manufacturers, including SamSung, Panasonic, BYD, and others, have adopted the 46XX format, incorporating various chemistries. This study presents a comprehensive analysis of BYD's 4680 lFP/graphite cylindrical lithium-ion cells. Detailed physical teardown, X-ray imaging, electrochemical testing, and electron imaging were performed to evaluate both cell- and materials-level attributes. The teardown and X-ray imaging reveal an uncommon multi-tab configuration and homogeneously double-sided electrode coatings, with no silicon additives in the graphite anode. Electrochemical testing indicates energy densities of 374.6 Wh l^{-1} and 150.5 Wh kg^{-1}. Furthermore, hybrid pulse power characterization and electrochemical impedance spectroscopy show impressive rate capability, with low cell-level DC area-specific resistance (6–17 $\Omega \cdot cm^2$ across various SOCs) and an area-specific charge transfer resistance of approximately 5.9 $\Omega \cdot cm^2$. These findings highlight a new direction for the 4680-cell format in both design and performance, establishing a strong foundation for future developments in large-format cylindrical battery technology.

 [DOI: 10.1149/1945-7111/ae1e33]

Manuscript submitted July 27, 2025; revised manuscript received September 17, 2025. Published November 26, 2025.

Supplementary material for this article is available online

Lithium-ion batteries (LIBs) have been at the forefront of consumer electronics applications over the past few decades and have since permeated the transportation sector through their use in electric vehicles (EVs), representing about 4% of the total passenger car fleet globally by the end of 2024—a figure expected to quadruple by 2030.[1] This growth will drive a surge in global battery demand, which surpassed 1 TWh in 2024. As EV adoption accelerates, battery and vehicle market prices will critically shape the landscape. For automotive applications, LIB development prioritizes cost, energy density, and power capability, while balancing safety and longevity. This has prompted exploration of diverse chemistries, cell formats, and integration strategies. EV batteries span from 18650 cylindrical cells (~3 Ah) to large-format pouch and prismatic cells exceeding 100 Ah, each with trade-offs in cycle life, thermal performance, energy density, and safety.[2,3]

Introduced by Tesla in 2020 for the Model Y platform, the 4680 cylindrical cell format (46 mm diameter, 80 mm length) is approximately five times larger in volume and capacity than the previously used 21700 cells. In conjunction with a tabless electrode design, these cells aim to enable higher energy densities without compromising manufacturing efficiency or production costs. Another dominant battery manufacturer, BYD, similarly employs an innovative cell format for its EV platforms—its proprietary Blade battery, a prismatic cell format utilizing lithium iron phosphate (LFP) chemistry that emphasizes safety, longevity, and cost-efficiency. However, BYD has also adopted and manufactured LFP/graphite batteries in the 4680 format for both its EV platforms and energy storage systems (ESS), with other battery OEMs also trending toward larger cell formats.

Despite growing commercial interest in large-format cells, manufacturers typically release only limited technical details. Cell chemistry and designs vary across suppliers and are shaped by proprietary manufacturing processes and customer specifications.[4] This contrasts with the small-scale cell formats generally used in academic research on LIBs, which can significantly influence cell characteristics compared to their commercial counterparts. The shift toward larger cell formats, combined with the limited availability of public data, underscores the need for detailed studies on commercial-scale cells. Prior publications that characterize state-of-the-art batteries have proven valuable for battery modeling and further research. For example, Baazouzi et al.[5] examined cylindrical LIBs from four manufacturers across four formats (18650, 20700, 21700, and 4680), focusing on design elements such as tab architecture and manufacturing quality. Subsequent work focusing on the Tesla 4680 cell from the Model Y was published by Ank et al.,[6] who conducted a methodical teardown and characterization to assess the cell at both the component and materials levels, revealing the application of lithium nickel manganese cobalt (NMC) oxide chemistry. More recently, Gorsch et al.[7] expanded upon the findings of Baazouzi et al.[5] and Ank et al.,[6] providing additional data on the design details of the Tesla 4680 cylindrical cell and directly comparing the following aspects with another state-of-the-art automotive battery cell, the BYD Blade:

1. Mechanical design
2. Material distribution
3. Material costs
4. Electrode material composition
5. Cell heating behavior

*Electrochemical Society Member.
**Electrochemical Society Fellow.
[z]E-mail: peter@glimp.se; shirleymeng@uchicago.edu

To the best of our knowledge, this is the second 4680-format cell type studied, following the Tesla 4680 reported by Ank et al. While LFP cylindrical LIBs are common in micromobility applications (i.e. Electric bikes, Electric scooters, etc) and consumer power tools, they remain rare in EV and EES applications, where prismatic formats are typically favored for having higher energy per cell and ease of pack assembly. As such, this study presents the first examination of an EV applications-ready cylindrical LFP cell. In contrast to the Tesla 4680, which uses NMC chemistry for higher energy and power demands, the use of LFP in a large cylindrical format over the more common prismatic format carries implications for the BYD 4680's power performance. Electrochemical testing confirms its classification as a power cell with a high-rate capability, as presented in subsequent portions of this study. Notably, this work analyzes 25 cells—providing a statistically meaningful dataset for evaluating cell-to-cell variation using computed tomography. Overall, this article aims to supplement the aforementioned works by providing insights into both the design and performance aspects of another relevant large-format cell—the BYD 4680 cylindrical LIB—as a basis for future optimization of LIB performance in both industrial and academic contexts.

Experimental

Cell teardown.—Prior to teardown, the cell was first discharged to 2.8 V. After opening the cylindrical cell, the entire electrode assembly was extracted from the casing for geometric measurements. The current collector disks at both the cathode and anode ends of the jelly roll were removed, and their dimensions, along with the overall structure of the assembly, were recorded. Adhesive tapes securing the jelly roll were detached, allowing the electrode stack to be fully unrolled. The thicknesses of the cathode and anode, including their current collector substrates, were measured using a digital micrometer (Mitutoyo 293), and electrode lengths were measured with a standard ruler.

X-ray imaging and 3D reconstruction.—A set of 25 cells was scanned and individually imaged using the Nikon XT H 225 ST 2x system located at Glimpse's facility. The system features a 225 kV rotating anode X-ray source and had been calibrated by a certified technician. Scans were conducted using Nikon's Inspect-X software with acquisition parameters optimized to achieve a balance between image quality and scan duration. Subsequent data processing and 3D reconstruction methodology are covered by Condon et al.[8]

Cell-level cycling and impedance analysis.—Open circuit voltage (OCV) and DC resistance measurements for all received cells were performed using Keithley 2400 source meters and are summarized in Table S1. Additionally, potentiostatic electrochemical impedance spectroscopy (PEIS) was conducted on two as-received cells using a BioLogic SP-200 potentiostat. The measurements covered a frequency range from 200 kHz to 100 mHz with six points per decade (logarithmic spacing) and a sinusoidal excitation voltage of 10 mV. These tests were carried out under conditions designed to minimize electromagnetic interference, employing ferrite cable shielding and an isolated test chamber (Espec BTX-475). The chamber was kept at an ambient temperature of 25 °C.

Capacity characterization was performed on the same two cells using a C/5 constant current charge-discharge protocol between 2.8 V and 3.6 V, followed by a constant voltage hold at 3.6 V until the current tapered to 0.25 A (equivalent to C/60). C-rates were calculated based on the nominal capacity of 15 Ah, as specified by the cell manufacturer.

Internal resistance across various states of charge (SOC) was further evaluated using Hybrid Pulse Power Characterization (HPPC). Two fresh cells underwent 10 s charge and discharge pulses at a 1 C rate, with a 3 h rest period between pulses, continuing until the voltage dropped to 2.8 V. Rate-capability testing was conducted on the same cells using symmetric charge-discharge cycles at C/2, 1 C, and 2 C under a constant current-constant voltage (CC-CV) protocol.

All cycling and HPPC measurements were performed using a high-current battery cycler equipped with a 60 A universal cylindrical cell holder (ARBIN Instruments) under an ambient temperature of 25 °C. Gravimetric and volumetric energy densities were calculated based on the measured discharge capacities and physical dimensions of the entire cell assembly.

Materials and elemental analysis.—To assess areal capacity loadings, circular electrode samples (13 mm for cathodes and 12.7 mm for anodes) were punched from the double-sided electrodes. One side of the cathode film was removed using *N*-methyl-2-pyrrolidone (NMP) to prepare single-sided electrodes and water was used to remove one side of the anode film. Coin-type half-cells employing LP57 electrolyte were then assembled to evaluate the single-sided areal capacity loadings at relatively low charge and discharge rates (C/5).

Scanning Electron Microscopy (SEM) was performed using an FEI Apreo system operated at 5 kV, with images acquired at various magnifications. The same instrument was used for energy-dispersive X-ray spectroscopy (EDS) to analyze the elemental composition of the electrodes. Samples for SEM and EDS were similarly prepared by punching circular electrode samples and cutting them to enable cross-sectional imaging.

Results and Discussion

Cell architecture and jelly roll design.—All cells investigated in this study were independently sourced from a reputable online cell supplier. Upon initial inspection prior to teardown, as shown in Fig. 1A, the BYD 4680 cylindrical cell was found to be insulated with a sleeve, in contrast to the Tesla 4680, which uses a nickel-plated steel can without direct insulation. Energy-dispersive spectroscopy (EDS) confirms similar use of nickel-plated steel for the BYD 4680 cell can, as the metal sheet exhibits a high Fe content in its cross-section and a high Ni content on its surface (Fig. S1). Furthermore, the BYD 4680 features a small pressure relief valve located adjacent to the cathode terminal. True to its format designation, the BYD 4680 cell measures 80 mm in height and 46 mm in diameter. Like the Tesla 4680, the can of the BYD 4680 functions as the negative terminal, with the cathode terminal (cathode lid) electronically isolated by a rubber gasket, as shown in Fig. 1B, where a white gasket is visible on the cathode lid labeled "3".

Prior to teardown, the cell was fully discharged to 2.8 V and transferred into an argon-atmosphere glovebox, where moisture and oxygen levels were maintained below 0.1 parts per million. Without removing the insulation sleeve, a pipe cutter—capable of cutting pipes up to 50 mm in diameter—was applied to the groove around the cathode lid. The cutter was gradually tightened to ensure that the blade penetrated only the metal housing and not the internal electrodes. After fully cutting through the can, it was observed that the cathode lid remained attached to a metallic cathode disk, as shown in Fig. 1B and labeled "1". Ceramic scissors were used to sever this connection, exposing the metallic cathode disk, the jelly roll, a blue plastic disk ("2" in Fig. 1B), and a plastic core mandrel in the jelly roll core ("5" in Fig. 1B). Similar to the metallic cathode disk, a metallic anode disk was found near the bottom of the cell housing ("4" in Fig. 1B), directly welded to the cell base. Before extracting the jelly roll, the bottom portion of the housing was removed with a pipe cutter, and the anode current collector tabs were similarly severed from the anode disk using ceramic scissors. At this stage, the jelly roll was disconnected from both the cathode lid and the cell housing bottom. However, the radial pressure exerted by the jelly roll against the sidewalls of the housing prevented straightforward removal. Consequently, a careful incision was made along the

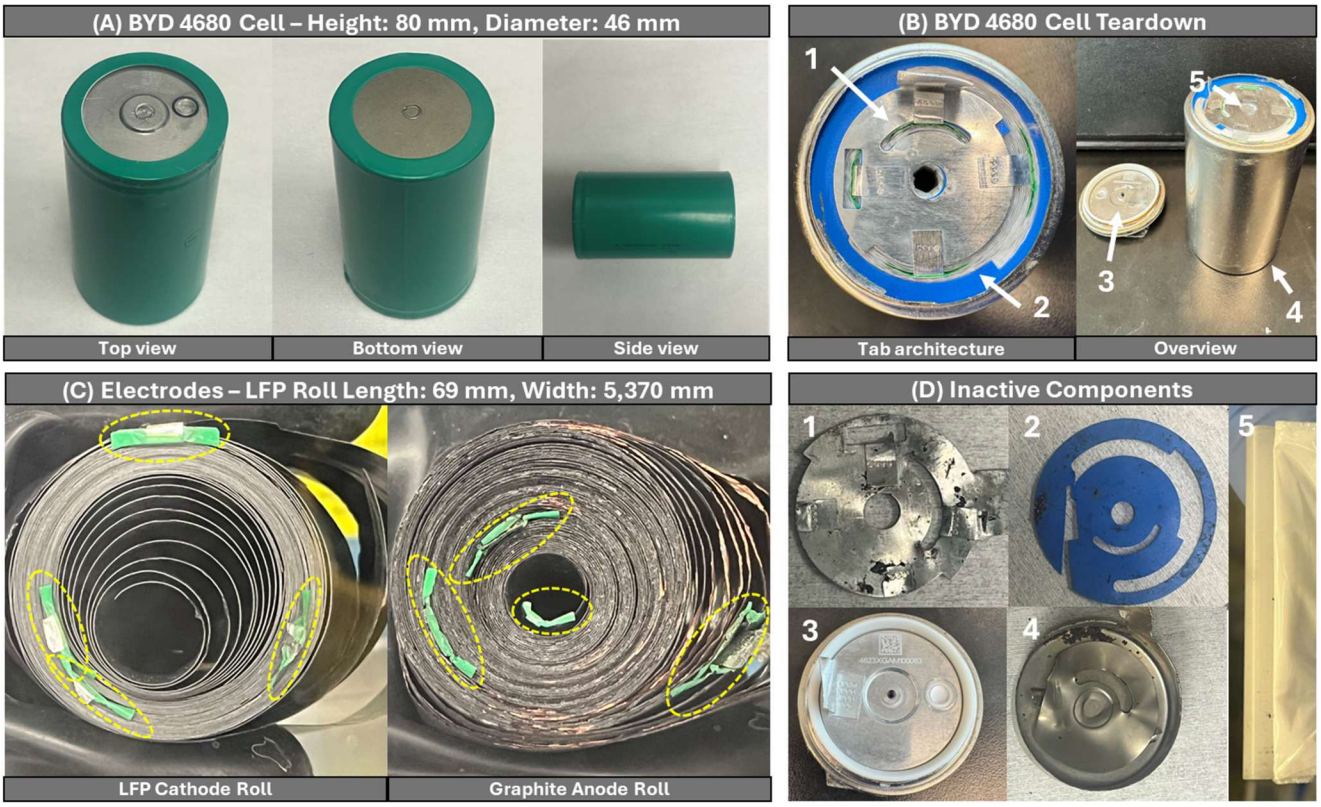

Figure 1. Overview of the BYD 4680 dimensions, teardown, internal features, and inactive components. (A) Cell dimensions and external view. (B) Cell can opening and tab architecture (Inactive cell components referenced 1–5 for (D). (C) LFP and graphite electrode rolls (Cathode and anode tabs highlighted in yellow dashed lines). (D) Inactive cell components: (1) Metallic cathode disk; (2) Plastic cathode disk; (3) Cathode lid; (4) Anode disk; (5) Plastic core mandrel.

sidewall of the casing—avoiding the electrodes—to relieve pressure. The metal casing was then peeled back using needle-nose pliers, enabling the jelly roll to be extracted for further analysis.

All cell components were subsequently measured after teardown and compared with the computed tomography scanning results discussed throughout this work.

After the jelly roll was extracted from the cell housing, the adhesive tapes were removed, and the jelly roll was unwound to reveal the distinct cathode, anode, and separators. The unwound electrode assembly is shown in Fig. 1C, displaying the separate LFP cathode roll and graphite anode roll. The dimensions of the LFP cathode roll were measured using a ruler, yielding a height of 69 mm and a width of 5,370 mm. The graphite anode roll was slightly taller at 71 mm with a width of 5,513 mm, which is 143 mm longer than the cathode. This corresponds to a height and width increase of approximately 2.90% and 2.66%, respectively. As highlighted in yellow, the LFP cathode roll includes four separate aluminum tabs, whereas the graphite anode roll has three separate nickel tabs. These tabs run along the length of each electrode and are largely covered by conventional polyethylene terephthalate (PET) film as confirmed by infrared spectroscopy against a pure PET powder reference (Fig. S2), which is wider than the tabs themselves. A multi-tab architecture is expected to alleviate internal resistance and improve current distribution uniformity, a more crucial parameter when considering the design of larger format cells.[9–11] Although highlighted, the nickel tab on the graphite roll located within the jelly roll core is fully covered by PET tape and not welded to anything. Therefore, no electrical connection is made between the cell body and the nickel tab. In addition to the electrode rolls, all other inactive cell components were extracted and are shown in Fig. 1D. The metallic cathode disk ("1") is 0.31 mm thick and exhibits an asymmetric design, with a larger outer diameter on approximately half the disk. It also features three cutouts—a circular center, a semicircular cutout, and a rectangular cutout—designed to accommodate the aluminum tabs and PET tapes. Between the metallic cathode disk and the cathode lid ("3") lies a blue plastic disk ("2"), hereafter referred to as the plastic cathode disk. Measuring 0.29 mm thick, this disk serves as an insulating barrier between the metallic cathode disk and the exposed copper current collector of the jelly roll, ensuring connection only to the positive terminal. Both the metallic cathode disk and plastic cathode disk share similar cutouts to allow passage of the aluminum tabs and PET tape. This arrangement is more clearly visible in the top-down view of the BYD 4680 in Fig. 1B, where the plastic cathode disk occupies a larger area than the metallic cathode disk. The four aluminum cathode tabs are welded to the metallic cathode disk at roughly 90° intervals. The metallic cathode disk itself is connected to the cathode lid via a primary weld tab. The positions of the aluminum tabs extend radially outward from the center of the jelly roll, with distances measured at 0.4 mm, 13.1 mm, 16.0 mm, and 18.3 mm, respectively. In contrast, the metallic anode disk ("4") is located at the bottom of the cell housing and is directly welded to the can, as opposed to being connected via a central tab. Compared to the metallic cathode disk, the metallic anode disk has a single semicircular cutout with a flat edge, rather than a fully rounded profile, and is of the same thickness at 0.31 mm. Like the aluminum cathode tabs, the nickel anode tabs also extend radially outward, with distances from the center measured at 9.0 mm, 15.6 mm, and 20.0 mm, and are welded directly to the metallic anode disk. Another plastic disk, identical in thickness to the plastic cathode disk, is placed between the anode disk and the jelly roll. It serves as an insulating barrier between the metallic anode disk and the exposed aluminum current collector of the jelly roll.

Finally, a plastic core mandrel ("5") was removed from the center of the jelly roll after the electrode assembly was unwound. This component serves as an anchoring point for the separator roll. This design is in stark contrast to that of the Tesla 4680, which, according to reports by Ank et al. and Gorsch et al., features an empty central cavity in the jelly roll rather than a traditional winding mandrel—a

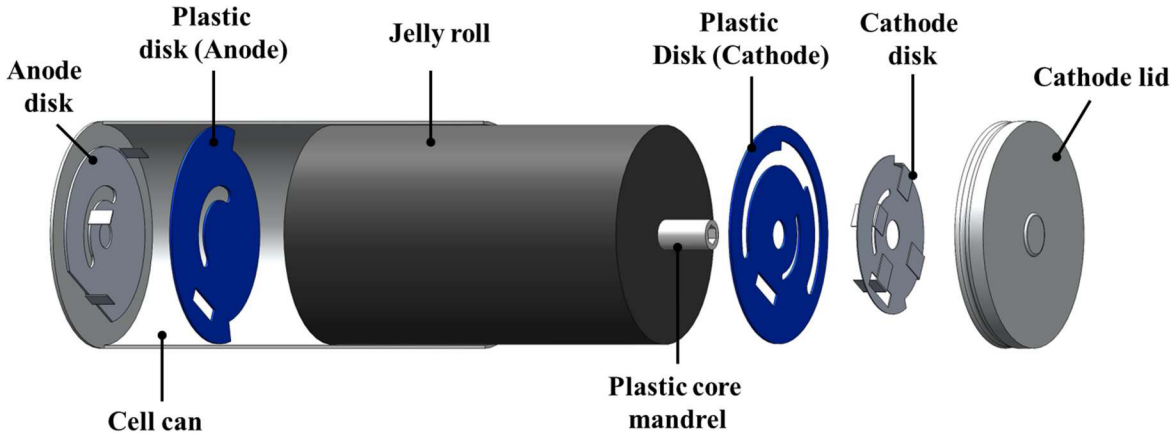

Figure 2. Exploded view of the BYD 4680. The schematic is drawn based on the measured dimensions of the components of the cell.

design approach common in many modern cylindrical cells. Figure 2 presents an exploded view of all relevant components within the BYD 4680 cell. As discussed above, metallic disks are used at both the cathode and anode ends, accompanied by their respective plastic disks to ensure electrical isolation—allowing the graphite anode to connect electrically with the cell housing and the LFP cathode to connect exclusively with the positive terminal (cathode lid). The plastic core mandrel fits snugly within the jelly roll core while the roll remains tightly wound.

To enable a more visual and quantitative analysis of the BYD 4680 cell structure, 3D X-ray imaging (computed tomography—CT) was employed as a nondestructive full-cell imaging technique. All scan data shown in Figs. 3 and 4 were previously published by Condon et al.,[8] where the experimental details regarding scan acquisition and data processing are discussed. The 2D radial (cross-sectional) slices of the BYD 4680, depicted in Fig. 3A, clearly illustrate the internal structure of the cell. The observed contrast can be correlated with the individual cell components described earlier. Upon closer inspection of the cross-sectional CT image, the contrast distinctly resolves the plastic core mandrel from the surrounding electrodes, as shown in Fig. 3B. Additionally, the cavity within the plastic core mandrel is visible, revealing a hexagonal design that was verified by optical inspection of the extracted component (right image in Fig. 3B). Axial (rotational) 2D slices presented in Fig. 3C offer a full-body image of the BYD 4680, where key internal regions are well resolved. As shown in Fig. 3D, a rotational CT slice reveals the layered electrode architecture, electrode overhangs, and structural features such as the current collector tabs at both the top and bottom of the cell. The high fidelity of the CT imaging is exemplified by the clear visualization of the electrolyte meniscus, as highlighted in the central image of Fig. 3D. The observed excess electrolyte in this particular cell prompted further investigation into the design and function of the plastic core mandrel. Physical measurements (Fig. S3A) show the mandrel is 7.1 mm tall, aligning well with the height of the graphite anode roll—and by extension, the jelly roll. The inclusion of a mandrel in cylindrical LIBs generally serves to stabilize the jelly roll by counteracting inward radial pressure or to provide a gas release pathway through a central hollow cavity in the event of thermal runaway.[12,13] To explore whether the plastic mandrel in the BYD 4680 serves functions beyond these conventional roles, ethanol was injected into the hexagonal cavity under ambient conditions to assess its permeability (**Supplementary Video 1**). No leakage was observed. More rigorous permeability testing was performed in an argon-atmosphere glovebox after vacuum drying the mandrel. It was weighed on a high-precision scale prior to full immersion in LP57 electrolyte for two weeks in a sealed container, then dried and reweighed. As summarized in Fig. S3B, the results indicate negligible electrolyte uptake, supporting the hypothesis that the mandrel primarily serves as structural reinforcement against jelly roll deformation during high-stress conditions such as fast charging or thermal events. **Supplementary Video 2** further demonstrates that the plastic mandrel is highly resistant to bending or cutting, highlighting its mechanical rigidity—an essential characteristic for mitigating jelly roll distortion. Additional infrared spectroscopy characterization, as shown in Fig. S4A, determined the core mandrel polymer composition to be polypropylene (PP) when compared to a polyethylene (PE) powder reference. The spectra clearly shows that characteristic vibrational modes of PE are absent in both the core mandrel. Specifically, characteristic CH_2 vibrational modes uniquely present in the PE monomer such as a rocking vibration (Fig. S4B) are not seen in the core mandrel spectra. Likewise, vibrational modes associated with the CH_3 functional group—unique to PP monomers—are not seen in the PE reference spectra (Figs. S4C, S4D). The harvested separator was also identified as PP in Fig. S4, with scanning electron microscopy (SEM) performed to inspect whether it was a monolayer or tri-layer structure, since the limited probing depth of infrared spectroscopy (Attenuated total reflectance) may not capture a potential polyethylene interlayer in the case of a tri-layer separator (Fig. S5). Typical sub-micron holes can be seen on the separator surface (Figs. S5A, S5B), and a monolayer architecture is elucidated given the homogeneity of the observed cross-section, as shown in Figs. S5C, S5D.

Consistent with CT imaging results, the length of the mandrel's hexagonal cavity measures 2.5 mm, with an approximate cross-sectional area of 16.24 mm^2 and a wall thickness of approximately 0.66 mm.

Varying the radial (cross-sectional) CT slices of the BYD 4680 enables more detailed inspection of the cell interior and its structural features. As shown in Fig. 4A, beginning with the bottommost cross-sectional slice ($Z = 0$), the metallic anode disk is clearly resolved, along with the welded connections to the anode's nickel tabs, which are highlighted in yellow in the corresponding image. Moving upward along the *Z*-axis ($Z > 0$), the four cathode aluminum tabs also become visible. The highlighted regions in the uppermost CT image of Fig. 4A correspond to the welded connections observed on the metallic cathode disk. Due to the difference in tab materials and corresponding X-ray absorption contrast, axial (rotational) CT slices of the cell, shown in Fig. 4B, readily distinguish the four cathode aluminum tabs (labeled C1, C2, C3, and C4) from the three anode nickel tabs (labeled A1, A2, and A3) throughout the rotation of the cell relative to the detector

To support rapid and automated analysis of CT scans from battery cells, Glimpse's image post-processing pipeline—as detailed in Condon et al.[8]—was employed to analyze the core structure of the BYD 4680. The jelly roll core was segmented (blue overlay in Fig. 4A), allowing for quantification of the core area and core circularity across a dataset of 25 BYD 4680 cells. Core circularity was calculated as the ratio of the minimum to maximum diameters obtained from an ellipse fit (D_{min}/D_{max}), serving as a key metric for

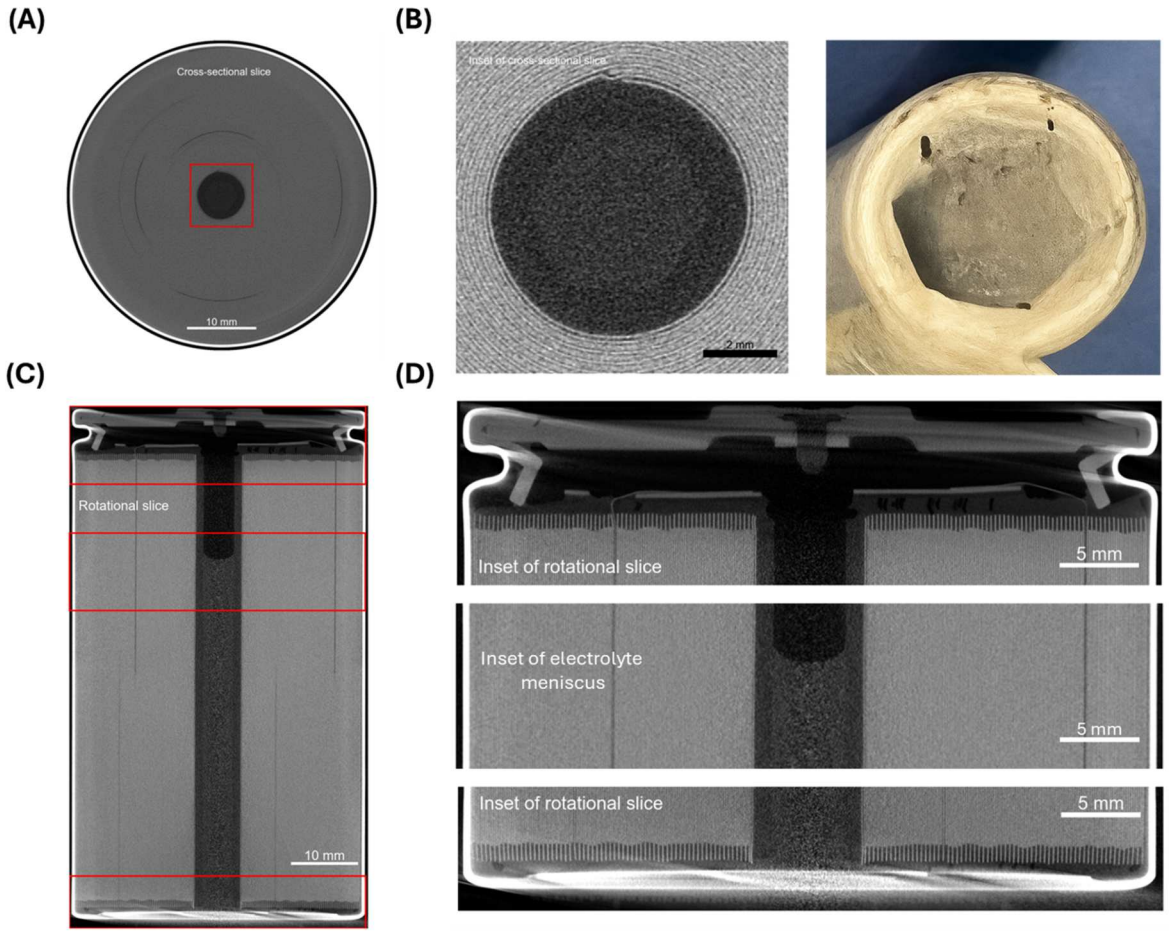

Figure 3. 3D X-ray imaging (Computed tomography—CT) of BYD 4680—Figure adapted from [Attia et al., Nature Communications, 2025] with modifications. (A) Cross-sectional CT slice. (Inset in red corresponds to magnification of CT image depicted in (B)). (B) Inset of cross-sectional slice highlighting jelly roll core (Left) and corresponding photograph of extracted plastic core mandrel (Right). (C) Rotational CT slice (Insets in red correspond to magnification of CT image depicted in (D)). (D) Inset of rotational slice highlighting cathode lid, electrode overhangs, and electrolyte meniscus.

assessing jelly roll buckling risk.[14,15] A high degree of uniformity in both core area and core circularity was observed across the 25 cells, with relative standard deviations (RSD) of 0.546% and 0.467%, respectively (Fig. 4C). Notably, the lowest core circularity value in the dataset was 97.2%, which is significantly higher than what is typically observed in conventional cylindrical cells. This high degree of uniformity underscores the potential advantages of cylindrical cell designs that incorporate a central core mandrel, particularly in enhancing mechanical stability and reducing deformation under stress.

Electrochemical testing.—Prior to electrochemical characterization, the as-received BYD 4680 cells were examined for their open circuit voltage (OCV) and DC resistance via an ohmmeter with results summarized in Table S1 to verify the cell consistency. All electrical characterizations presented in this section were conducted on two separate cells to ensure repeatability. The capacity and nominal discharge voltage of the BYD 4680 were measured using a constant current (CC) protocol at C/5, based on a nominal capacity of 15 Ah (3 A), followed by a constant voltage (CV) cutoff at C/60 (0.25 A). Initial discharge measurements revealed that the cells were shipped at approximately 20% state of charge (SOC). The cells were subsequently charged and discharged at the same C/5 rate between 2.8 V and 3.65 V. As shown in Fig. 5A, the cells delivered a discharge capacity of 15.41 Ah and a discharge energy of 49.82 Wh, corresponding to an average discharge voltage of 3.2 V. Characteristic voltage plateaus associated with graphite staging and the $FePO_4$ (FP) ↔ $LiFePO_4$ (LFP) phase transformation were clearly observed, confirming the LFP/graphite cell chemistry.[16,17] Based on the measured weight and volume of the BYD 4680 cell, the gravimetric and volumetric energy densities were calculated to be 151 Wh kg^{-1} and 374.6 Wh l^{-1}, respectively. When compared to the Tesla 4680 at the cell level, the Tesla cell exhibits approximately 1.6× higher gravimetric and 1.7× higher volumetric energy density (Table S2). The lower energy density of the BYD 4680 is consistent with the intrinsic limitations of the LFP cathode, which has lower specific energy than NMC-based chemistries. Additionally, the longer LFP cathode roll in the BYD 4680 (5,370 mm) compared to the NMC cathode roll in the Tesla 4680 (3,215 mm), as reported by Gorsch et al., contributes to an increased amount of inactive material at the cell level. These include aluminum and copper current collectors, separator film, conductive carbon, and binder material. The same cells from Fig. 5A were subjected to continuous cycling under identical conditions without rest periods between cycles, as illustrated in Fig. 5B. Both cells demonstrated stable capacity retention with less than 0.1% capacity fade over 10 cycles, along with an increasing coulombic efficiency (CE), indicating stabilization behavior during early cycling.

To accurately assess the areal capacity loadings of the electrodes, single-sided portions of the LFP cathode roll and graphite anode roll extracted from the BYD 4680 were prepared by mechanical scraping. Disks measuring 13 mm in diameter for the LFP cathode and 12.7 mm for the graphite anode were then punched and assembled into coin-type half-cells using LP57 electrolyte. Electrochemical cycling of the LFP and graphite half-cells was performed at a C-rate of C/10, yielding characteristic single-plateau

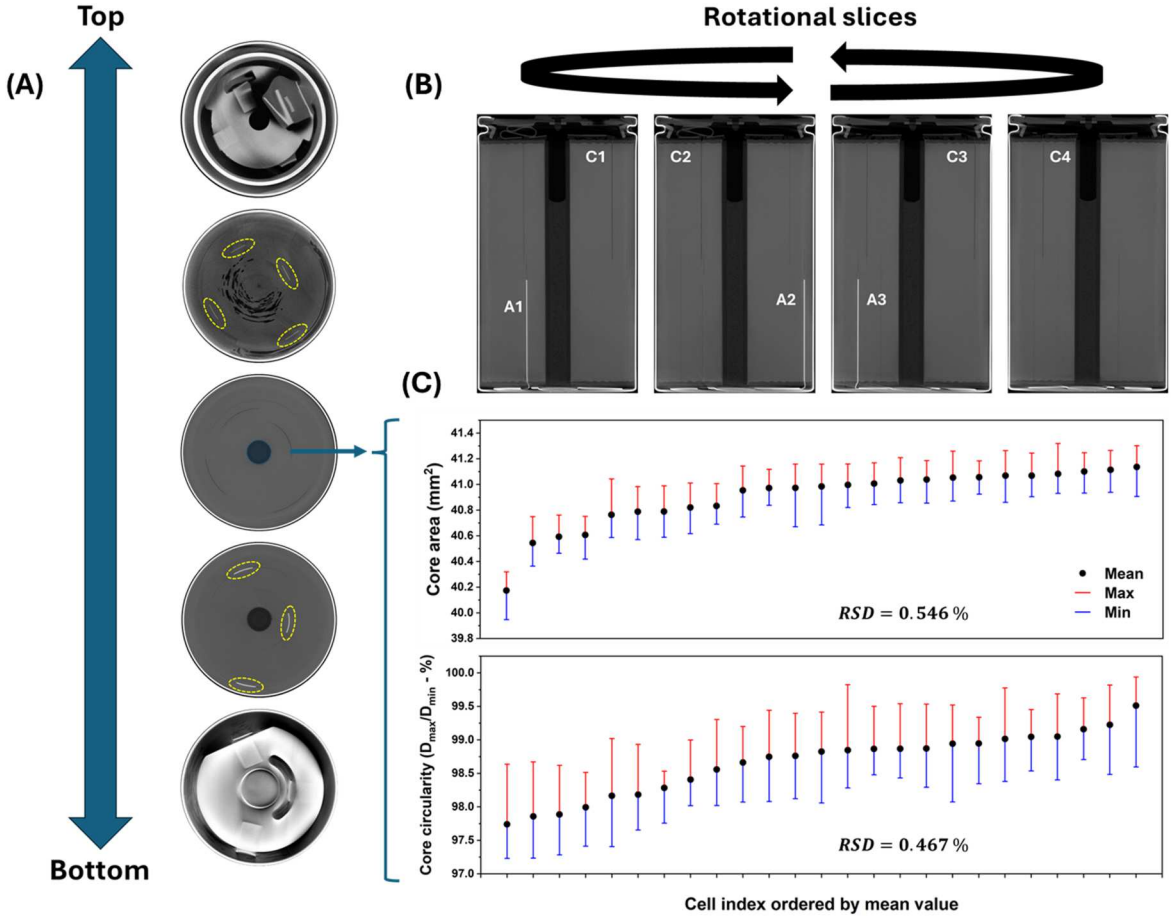

Figure 4. 3D X-ray imaging (CT) of BYD 4680—Cell features and uniformity. (A) Cross-sectional CT slices with varying depth (Highlighted regions of cathode and anode tabs in yellow dashed lines). (B) Rotational CT slices with varying angles, 4 cathode tabs (C1,2,3,4) and 3 anode tabs (A1,2,3) are labelled. (C) Core area (mm^2) and core circularity (D_{min}/D_{max}) metrics across 25 scanned BYD 4680 ordered by mean values (Metrics evaluated from overlay of jelly roll core in blue as shown in A), and cell indices between the two plots do not correspond to one another (Order of core area does not match order of core circularity).

and multi-plateau voltage profiles for the two materials, respectively (Fig. 5C). Subsequent cycling at C/5 produced average reversible capacities of 2.77 mAh for the LFP cathode and 2.96 mAh for the graphite anode (Fig. 5D). Based on their respective electrode areas, these values correspond to average single-sided areal capacities of 2.09 mAh cm^{-2} for the LFP cathode and 2.34 mAh cm^{-2} for the graphite anode, resulting in an N/P ratio of 1.1. The slight variation observed in the delivered capacities of the LFP cathode half cells is attributed to potential damage incurred during the removal of one electrode side. Nonetheless, upon continued cycling at C/5, the half cells exhibited stable performance, with consistent CE between LFP half cells, as shown in Fig. 5D.

Impedance measurements of the as-received BYD 4680 were conducted using an Arbin cylindrical cell holder with circuit resistance below 5 mΩ and a Bio-Logic potentiostat. Galvanostatic electrochemical impedance spectroscopy (EIS) with a 500 mA excitation amplitude revealed a milliohm-level impedance at 20% SOC (Fig. 6A). The impedance spectra were fitted using a conventional Randles equivalent circuit model, resulting in an area-specific ionic resistance R_s of 51.5 Ω·cm^2 and an area-specific charge transfer resistance R_{CT} of 5.9 Ω·cm^2. As the charge transfer resistance encompasses both lithium-ion transport kinetics through the solid electrolyte interphase (SEI) and charge exchange kinetics at the active material surface, the low R_{CT} value is expected considering the cell has not been subjected to long-cycling. To further characterize the cell's resistance behavior, hybrid pulse power characterization (HPPC) was performed to evaluate DC resistance as a function of SOC (Fig. 6B). The HPPC protocol involved the following steps: charging to 3.65 V at C/5, followed by a 1 h rest; discharging at C/2 for 24 min (resulting in a 20% SOC drop); a 3 h rest; and application of 10 s charge and discharge pulses at 1 C (15 A). This sequence of C/2 discharge, 3 h rest, and 10 s 1 C pulses was repeated until the cells reached the lower cutoff voltage of 2.8 V. During each 10 s pulse, cell voltage and current (for both charging and discharging) were recorded at one-second intervals, yielding 10 data points per pulse. The DC resistance for each interval was calculated using Ohm's law. The average DC resistance values across the pulse durations for two BYD 4680 cells subjected to HPPC testing are summarized in Fig. 6C. In general, DC resistance is observed to increase with decreasing SOC in both the charging and discharging directions; however, the increase is more pronounced in the discharge direction, particularly in the mid-to-low SOC regions. Based on previous teardown analyses of commercial NMC and NCA systems, the SOC-dependent impedance behavior is likely associated with the nonlinear nature of charge transfer reactions.[18] In comparison, LFP cells tend to exhibit a relatively lower sensitivity of impedance to SOC.[19]

Owing to the well-known trade-off between energy and power in LIBs, the rate capability of the BYD 4680 cells was assessed.[20] This is of particular interest given that fast charging of LFP batteries may offer a promising solution to alleviating range anxiety in automotive applications, especially when compared to high-nickel NMC systems.[21–23] Symmetrical charge/discharge rates of C/2, 1 C, and 2 C—corresponding to 7.5 A, 15 A, and 30 A, respectively, based on the nominal capacity of 15 Ah—were evaluated for 5 cycles. A constant voltage (CV) step was applied after the constant current (CC) phase until a C/60 cutoff current (0.25 A) was reached, consistent with earlier testing procedures. The tested cells exhibited

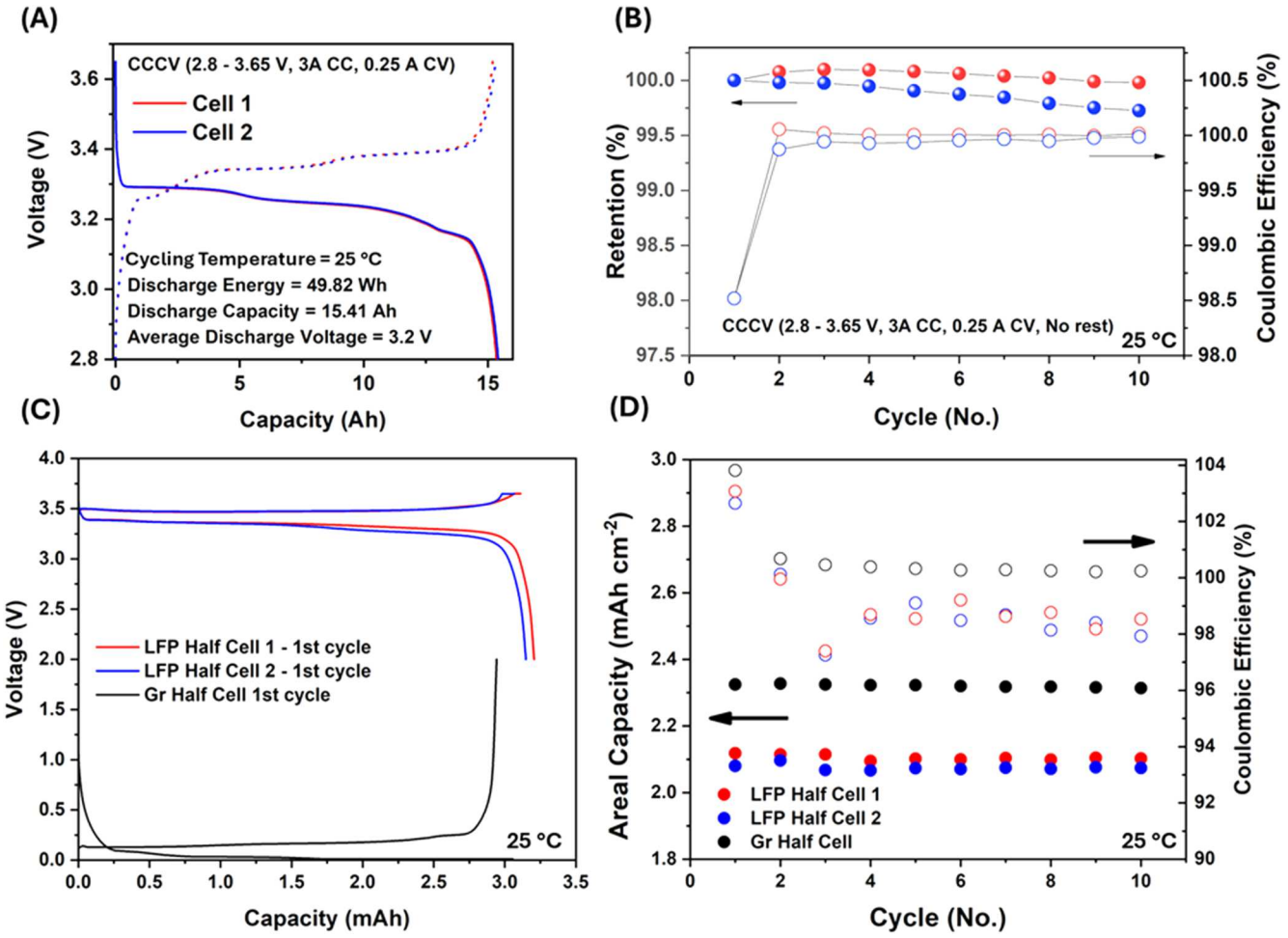

Figure 5. Electrochemical evaluation of full cell level and electrode (half-cell) level performance under 25 °C. (A) Galvanostatic cycling of as-received BYD 4680 lFP/graphite cylindrical lithium-ion battery at C/5. (B) Multi-cycle stability of the BYD 4680 cells at C/5. (C) 1st cycle evaluation of LFP cathode and graphite anode in half-cells at C/10. (D) Multi-cycle stability of the LFP cathode and graphite anode half-cells at C/5 following an initial cycle at C/10.

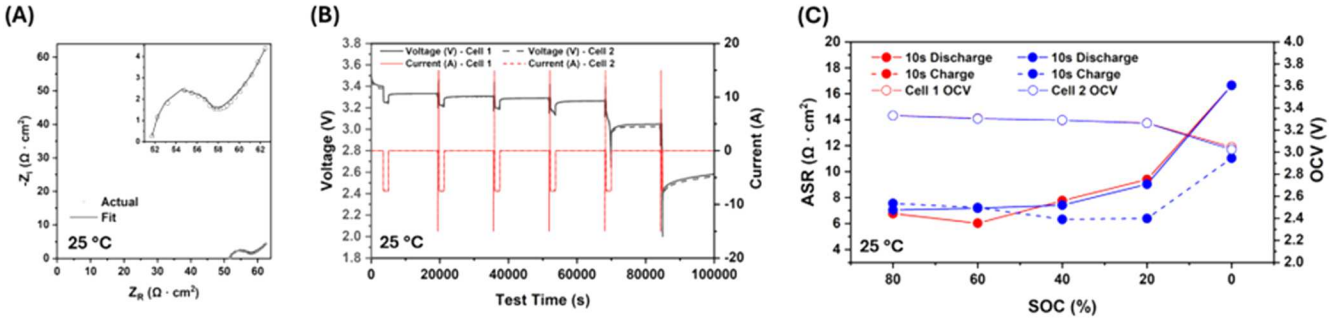

Figure 6. Impedance and pulse resistance evaluation of the measured cells normalized to the LFP electrode area at 25 °C. (A) Impedance spectra as received (20% SOC). (B) Hybrid pulse power characterization testing employing 10 s charge and discharge pulses at 1 C from 80% SOC to 0% SOC. (C) DC area-specific pulse resistances across SOCs in charge and discharge direction.

good reproducibility, as evidenced by the overlapping voltage profiles in Fig. 7A. As expected, the capacity contribution from the CV step increased with higher C-rates. This behavior is attributed to incomplete lithiation of the graphite anode or incomplete delithiation of the LFP cathode at high rates, leading to reduced overall capacity utilization—from approximately 15.00 Ah at C/2 to 13.25 Ah at 2 C. However, upon returning to C/2 in subsequent cycles, the reversible capacity is nearly 15 Ah after 5 cycles (Fig. 7B). These results underscore the high-power capability of the BYD 4680, with 94.7% and 87.9% capacity utilization at C-rates of 1 C and 2 C, respectively, based on discharge capacities measured on the 5th cycle. It is important to note that after the 1st cycle at increasing rates, the CE stabilizes to 99.8% at both 1 C and 2 C, further reinforcing the cell's impressive rate capability. Comparing the fast-charging capabilities of the BYD 4680 and the Tesla 4680 (as reported by Ank et al.), the BYD 4680 achieved 97.8% and 92.7% of its nominal charging capacity at 1 C and 2 C, respectively, while the Tesla 4680 reached 82.8% and 71.0% at the same rates (Considering a single cycle at these C-rates and under identical testing temperatures of 25 °C)—highlighting the BYD 4680 as a high-performance power cell. It is anticipated that continuous high-rate charging ($\geqslant$2 C = 30 A) may generate substantial heat,

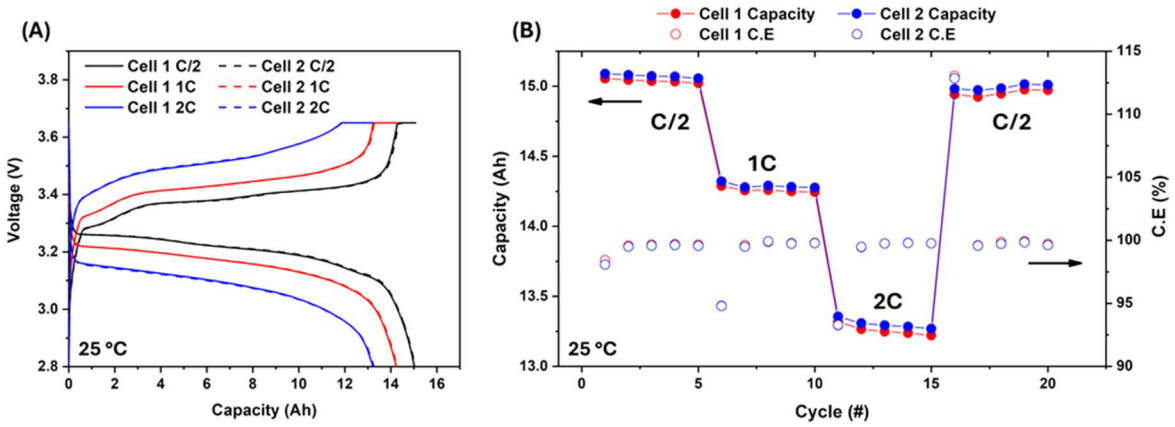

Figure 7. Rate capability evaluation of the measured cells at 25 °C. (A) Voltage vs capacity profiles across symmetrical charge and discharge rates of C/2, 1 C, and 2 C. (B) Capacity vs cycles summary at different C-rates.

potentially reducing the risk of lithium metal plating on the graphite anode. However, additional side reactions may also occur, excessively forming SEI. These side reactions are typically absent during fast discharging, as they are driven by the low electrode potentials present during charging.

Materials characterization.—For a more detailed analysis of the LFP and graphite electrodes, SEM was performed, with Fig. 8 depicting both top-down and cross-sectional views of both the cathode and anode material.

On the cathode side, the electrode thickness measures approximately 150 μm, with an aluminum current collector around 10 μm thick, as observed in the cross-sectional SEM image (Fig. 8A). These measurements are in excellent agreement with those obtained via micrometer readings and rotational CT slice analysis. From the top-down view shown in Fig. 8B, nano-sized cathode particles are visible, ranging from approximately 100 to 300 nm in diameter. These morphological features are characteristic of nano-structured $LiFePO_4$ (LFP) materials, which are engineered to enhance rate performance by reducing lithium-ion diffusion lengths compared to their micron-sized counterparts.[24] The LFP chemistry is confirmed by EDS, which reveals atomic ratios of Fe, P, and O close to 1:1:4 (Fig. S6). In addition, a clear contrast in image intensity distinguishes the larger, micron-sized carbon particles due to their superior electronic conductivity relative to the surrounding nano-LFP particles. Carbon coatings on LFP primary particles are commonly applied to compensate for LFP's inherently low electronic conductivity, thereby facilitating charge transfer.[25] While the larger carbon particles are readily apparent, the carbon coating on the LFP particles is not well resolved, as it is typically thinner than 10 nm. Notably, EDS analysis also indicates the presence of Ti, detected at an atomic ratio of approximately 0.3% (considering only Fe, P, O, and Ti). This likely points toward Ti doping as previous studies have shown that appropriate Ti doping in LFP can slightly reduce lattice spacing,[26]

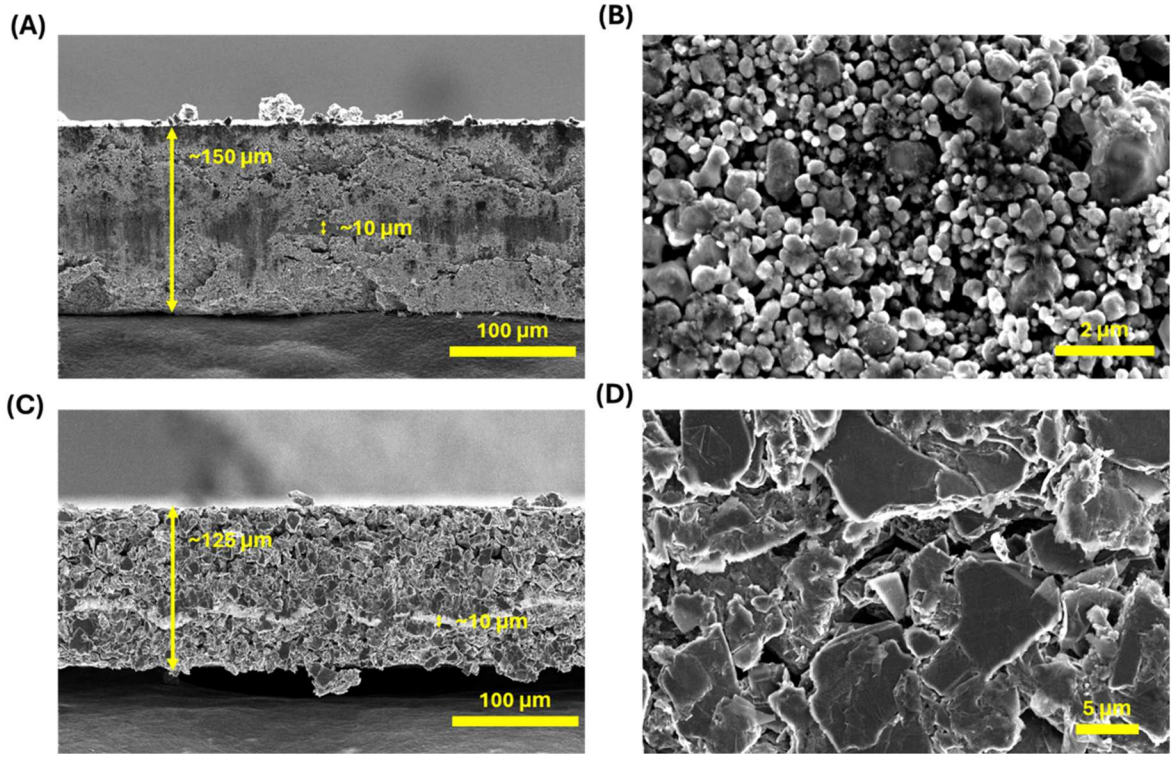

Figure 8. Representative SEM images of the double-sided electrodes as harvested from the teardown cell. SEM images of the LFP cathode from the (A) cross-sectional and (B) surface view, and the graphite anode from the (C) cross-sectional and (D) surface view. Additional SEM images and elemental composition via EDS can be found in supplementary information.

thereby shortening lithium-ion diffusion paths—an effect that, when combined with nano-structuring, may enhance electrochemical performance.

The anode layer measures approximately 125 μm thick, with a copper current collector around 10 μm thick, as shown in Fig. 8C. These values are consistent with average values obtained from micrometer measurements conducted at five points across the jelly roll and with CT data. To determine whether coating thickness differs between the inner and outer sides of the jelly roll—potentially to mitigate the risk of delamination at a tight bend radius—additional single-sided thickness measurements were performed after carefully wiping off the graphite coating with water on both inner and outer electrode layers. These measurements revealed that the graphite coating is uniform on both sides. Compared to the single-sided graphite anode coating in the Tesla 4680 (as reported by Gorsch et al.), the BYD 4680 features a coating thickness of 54.5 μm—a 54% reduction. While partly due to the lower energy density of LFP, the significantly thinner graphite anode also reduces ohmic resistance, enhances lithium-ion diffusion, and improves thermal dissipation—all of which facilitate fast charging and high-power output, as shown in the rate-testing results. Top-down SEM imaging (Fig. 8D) reveals that the anode is composed of flake-like graphite particles with diameters up to 10 μm. EDS analysis confirms the exclusive use of graphite as the active material, with no detectable silicon. A carbon atomic ratio of 91.2% was measured (Fig. S7), consistent with graphite content as well as the presence of conductive additives like carbon black and polymeric binders. A sodium atomic ratio of 1.8% suggests the possible use of sodium carboxymethyl cellulose (CMC) as a binder. Recently, dry-processed electrode manufacturing has been explored for achieving high areal mass loading via polymer fibrillation in the dry mixing of active and conductive materials.[27] However, no fiber-like morphology was observed in either the cathode or the anode. This suggests that both electrodes were likely fabricated using conventional slurry-based methods.

Conclusions

This article presents a comprehensive analysis on the design and characteristics of a BYD 4680 cylindrical lithium-ion battery with LFP chemistry. The study spans both the cell and components level through a detailed teardown in conjunction with electrochemical analysis and state-of-the-art CT imaging. The cell teardown revealed double-sided cathodes and anodes, with a plastic core mandrel featuring a hexagonal cavity. Multi-tab architecture is observed for both the cathode and anode, notably with a core tab on the anode roll not electronically connected to the cell terminal. Mechanical and permeability testing of the mandrel revealed no further functions beyond conventional support for jelly roll deformation. CT analysis showed exceptionally high uniformity in jelly roll core area and circularity across the cells. SEM revealed nano-sized LFP spherical particles on the cathode and flake graphite particles on the anode. EDS analysis revealed Ti doping of the LFP cathode particles as well as the exclusive application of graphite as the anode material, with no detectable silicon. No fiber-like morphology was seen for either the cathode or anode, suggesting the conventional slurry-based processing of the electrodes, in contrast to next-generation solvent-free electrode processing techniques. At the cell level, volumetric and gravimetric energy densities were calculated as 374.6 Wh l^{-1} and 150.5 Wh kg^{-1}, respectively. Impedance testing reveals milliohm level resistance associated with Li-ion charge transfer. HPPC testing similarly revealed milliohm level DC resistance, with pronounced increases into the low-SOC regions. Symmetric charge and discharge rate testing of the cells shows good capacity utilization, with 94.8% and 88.1% at 1 C and 2 C, with respect to capacities obtained at C/2. In conjunction with the exceptionally thin graphite anode architecture, these results affirm its classification as an impressive high-power cell.

These findings shed light on the design, materials, and performance characteristics of large-format cylindrical lithium-ion cells with LFP chemistry—an increasingly promising direction for both EV and EES applications. The 4680 cell format marks an exciting evolution in cylindrical cell design, and as a major cell producer, BYD introduces a distinctly different approach from Tesla's 4680, featuring a unique multi-tab configuration and mandrel-supported architecture. This work not only demonstrates the viability of LFP in high-power cylindrical formats but also establishes a valuable reference point for future innovation. It identifies opportunities for further investigation, including thermal behavior and cathode surface engineering, and sets the stage for advancing cylindrical lithium-ion battery technology beyond traditional boundaries.

Acknowledgments

This work is supported by the discretion fund by Sustainable Power and Energy Center at UC San Diego. Special thanks to Shaojie Yang and David Gonsoulin for the electrical measurements at the Center for Energy Research at UC San Diego. The SEM-EDS in this work were performed at the San Diego Nanotechnology Infrastructure (SDNI) of UC San Diego, which is supported by the National Science Foundation (Grant ECCS-1542148). Y.S.M. acknowledges the partial support from the startup funding at University of Chicago.

Declaration of Interests

A.C. and P.M.A. have a financial interest in Glimpse Engineering Inc., which specializes in high-throughput CT scanning for batteries.

Authors' Contributions

A.L., W.Y., P.M.A., and Y.S.M. designed the experiments. A.L. and W.Y. performed impedance measurements and cell teardown. W.Y. conducted the SEM-EDS measurements and electrochemical testing at half-cell level. S.Y. and D.G. conducted the electrochemical testing at the full-cell level. A.L. analyzed all data and prepared the manuscript. All authors contributed to the discussion and provided feedback on the manuscript.

ORCID

Alex Liu https://orcid.org/0009-0008-4584-7324
Amariah Condon https://orcid.org/0009-0001-0774-8623
Peter M. Attia https://orcid.org/0000-0003-4745-5726
Ying Shirley-Meng https://orcid.org/0000-0001-8936-8845

References

1. (2025), IEA (2025), Global EV Outlook 2025, IEA, Paris https://www.iea.org/reports/global-ev-outlook-2025, Licence: CC BY 4.0.
2. Y. Miao, P. Hynan, A. Von Jouanne, and A. Yokochi, "Current Li-ion battery technologies in electric vehicles and opportunities for advancements." *Energies*, **12**, 1074 (2019).
3. R. Schmuch, R. Wagner, G. Hörpel, T. Placke, and M. Winter, "Performance and cost of materials for lithium-based rechargeable automotive batteries." *Nat. Energy*, **3**, 267 (2018).
4. M. Ank, T. Kröger, M. Schreiber, and M. Lienkamp, "Experimental analysis of lithium-ion cell procurement: quality differences, correlations, and importance of cell characterization." *Journal of Energy Storage*, **66**, 107430 (2023).
5. S. Baazouzi, N. Feistel, J. Wanner, I. Landwehr, A. Fill, and K. P. Birke, "Design, properties, and manufacturing of cylindrical Li-ion battery cells—a generic overview." *Batteries*, **9**, 309 (2023).
6. M. Ank et al., "Lithium-ion cells in automotive applications: tesla 4680 cylindrical cell teardown and characterization." *J. Electrochem. Soc.*, **170**, 120536 (2023).
7. J. Gorsch, J. Schneiders, M. Frieges, N. Kisseler, D. Klohs, H. Heimes, A. Kampker, M. M. Castro, and E. Siebecke, "Contrasting a BYD Blade prismatic cell and Tesla 4680 cylindrical cell with a teardown analysis of design and performance." *Cell Reports Physical Science*, **6**, 102453 (2025).
8. A. Condon, B. Buscarino, E. Moch, W. J. Sehnert, O. Miles, P. K. Herring, and P. M. Attia, "A dataset of over one thousand computed tomography scans of battery cells." *Data in Brief*, **55**, 110614 (2024).
9. W. Zhao, G. Luo, and C. Y. Wang, "Effect of tab design on large-format Li-ion cell performance." *J. Power Sources*, **257**, 70 (2014).
10. S. Li et al., "Optimal cell tab design and cooling strategy for cylindrical lithium-ion batteries." *J. Power Sources*, **492**, 229594 (2021).
11. M. F. Börner, A. M. Mohsseni, N. De, M. Faber, F. Krause, W. Li, S. Bihn, F. Ringbeck, and D. U. Sauer, "Manufacturing cost comparison of tabless vs

standard electrodes for cylindrical lithium-ion batteries." *Journal of Energy Storage*, **77**, 109941 (2024).
12. K. Tagawa and R. J. Brodd, "Production processes for fabrication of lithium-ion batteries." *In Lithium-Ion Batteries: Science and Technologies*, **8**, 181 (2009).
13. D. P. Finegan et al., "Identifying the cause of rupture of Li-Ion batteries during thermal runaway." *Adv. Sci.*, **5**, 1700369 (2018).
14. S. D. Gelam, S. Maddipatla, C. Chicone, and M. Pecht, "Core collapse in cylindrical Li-ion batteries." *J. Power Sources*, **623**, 235471 (2024).
15. L. Willenberg, P. Dechent, G. Fuchs, M. Teuber, M. Eckert, M. Graff, N. Kürten, D. U. Sauer, and E. Figgemeier, "The development of jelly roll deformation in 18650 lithium-ion batteries at low state of charge." *J. Electrochem. Soc.*, **167**, 120502 (2020).
16. Y. Preger, H. M. Barkholtz, A. Fresquez, D. L. Campbell, B. W. Juba, J. Romàn-Kustas, S. R. Ferreira, and B. Chalamala, "Degradation of commercial lithium-ion cells as a function of chemistry and cycling conditions." *J. Electrochem. Soc.*, **167**, 120532 (2020).
17. M. Dubarry and B. Y. Liaw, "Identify capacity fading mechanism in a commercial LiFePO4 cell." *J. Power Sources*, **194**, 541 (2009).
18. L. Chen, M. Zhang, Y. Ding, S. Wu, Y. Li, G. Liang, H. Li, and H. Pan, "Estimation the internal resistance of lithium-ion-battery using a multi-factor dynamic internal resistance model with an error compensation strategy." *Energy Reports*, **7**, 3050 (2021).
19. M. K. Tran, A. DaCosta, A. Mevawalla, S. Panchal, and M. Fowler, "Comparative study of equivalent circuit models performance in four common lithium-ion batteries: LFP, NMC, LMO, NCA." *Batteries*, **7**, 51 (2021).
20. M. Quarti, A. Bayer, and W. G. Bessler, "Trade-off between energy density and fast-charge capability of lithium-ion batteries: A model-based design study of cells with thick electrodes." *Electrochemical Science Advances*, **3**, e2100161 (2023).
21. A. Masias, J. Marcicki, and W. A. Paxton, "Opportunities and challenges of lithium ion batteries in automotive applications." *ACS Energy Lett.*, **6**, 621 (2021).
22. M. Al-Saadi, J. Olmos, A. Saez-de-Ibarra, J. Van Mierlo, and M. Berecibar, "Fast charging impact on the lithium-ion batteries' lifetime and cost-effective battery sizing in heavy-duty electric vehicles applications." *Energies*, **15**, 1278 (2022).
23. B. Bose, A. Garg, B. K. Panigrahi, and J. Kim, "Study on Li-ion battery fast charging strategies: Review, challenges and proposed charging framework." *Journal of Energy Storage*, **55**, 105507 (2022).
24. Z. Ju, X. Xu, X. Zhang, K. U. Raigama, and G. Yu, "Towards fast-charging high-energy lithium-ion batteries: From nano-to micro-structuring perspectives." *Chem. Eng. J.*, **454**, 140003 (2023).
25. J. Wang and X. Sun, "Understanding and recent development of carbon coating on $LiFePO_4$ cathode materials for lithium-ion batteries." *Energy Environ. Sci.*, **5**, 5163 (2012).
26. Z. Li, X. Ren, Y. Zheng, W. Tian, L. An, J. Sun, R. Ding, L. Wen, and G. Liang, "Effect of Ti doping on $LiFePO_4$/C cathode material with enhanced low-temperature electrochemical performance." *Ionics*, **26**, 1599 (2020).
27. W. Jin, G. Song, J. K. Yoo, S. K. Jung, T. H. Kim, and J. Kim, "Advancements in dry electrode technologies: Towards sustainable and efficient battery manufacturing." *ChemElectroChem*, **11**, e202400288 (2024).